Chemical Science

Accepted Manuscript

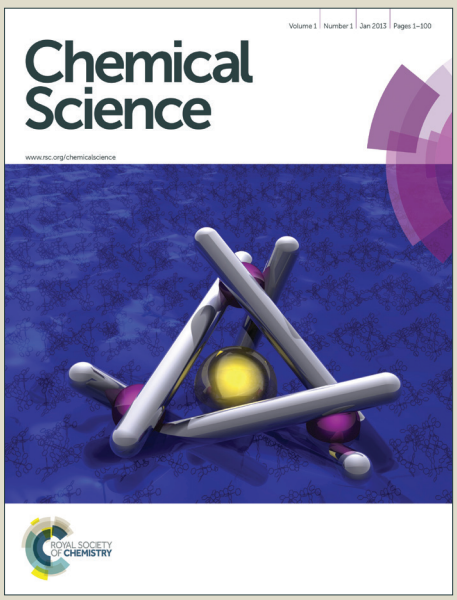

ROYAL SOCIETY OF CHEMISTRY

www.rsc.org/chemicalscience

Cite this: DOI: 10.1039/c0xx00000x

www.rsc.org/xxxxxx

ARTICLE TYPE

A pH-activatable and aniline-substituted photosensitizer for near-infrared cancer theranostics†

Jiangwei Tian,‡ Jinfeng Zhou, ‡Zhen Shen, Lin Ding, Jun-Sheng Yu and Huangxian Ju*

Received (in XXX, XXX) Xth XXXXXXXXX 20XX, Accepted Xth XXXXXXXXX 20XX

DOI: 10.1039/b000000x

This work reports a newly designed pH-activatable and aniline-substituted aza-boron-dipyrromethene as a trifunctional photosensitizer to achieve highly selective tumor imaging, efficient photodynamic therapy (PDT) and therapeutic self-monitoring through encapsulating it in a cRGD-functionalized nanomicelle. The diethylaminophenyl is introduced to the structure for pH-activatable near-infrared fluorescence and singlet oxygen ($^1O_2$) generation, and bromophenyl is imported to increase the $^1O_2$ generation efficiency upon pH activation in virtue of its heavy atom effect. After encapsulation, the nanoprobe can target to $\alpha_v\beta_3$ integrin-rich tumor cells via cRGD and be activated by physiologically acidic pH for cancer discrimination and PDT. The fascinating advantage of nanoprobe is near-infrared implementation beyond 800 nm, which significantly improves the imaging sensitivity and increases the penetration depth of PDT. By monitoring the fluorescence decrease in tumor region after PDT, the therapeutic efficacy is reflected *in situ* and in real time, which provides a valuable and convenient self-feedback function for PDT efficacy tracking. Therefore, this rationally designed and carefully engineered nanoprobe offers a new paradigm for precise tumor theranostics and may provide novel opportunities for future clinical cancer treatment.

Introduction

In current cancer research, the design of theranostic agent that combines diagnosis and therapy into a single platform offers exciting prospects for the development of personalized medicine.[1] Many well established photosensitizers of the first, second and third generation[2a] have been used for the construction of theranostic agents.[2] They are generally nontoxic in native state, however, under irradiation with appropriate wavelength and power, can transfer the absorbed photon energy to surrounding molecular oxygen ($^3O_2$), generating cytotoxic singlet oxygen ($^1O_2$) to kill cancer cells.[3] This technology is well known as photodynamic therapy (PDT) and has been largely used for the treatment of many localized superficial cancers.[3] Meanwhile, upon light excitation, the photosensitizer can emit fluorescence for tumor diagnosis, location and image-guided therapy.[4] Furthermore, by measuring the fluorescence photobleaching of photosensitizer or detection of $^1O_2$ phosphorescence emission during PDT process,[5] the light dose in PDT can be accurately administered to prevent under- or over-illumination.

State Key Laboratory of Analytical Chemistry for Life Science, State Key Laboratory of Coordination Chemistry, School of Chemistry and Chemical Engineering, Nanjing University, Nanjing 210093, P.R. China. Fax/Tel.: +86 25 83593593;E-mail: hxju@nju.edu.cn.

† Electronic Supplementary Information (ESI) available: Experimental details andsupplementary figures. See DOI:10.1039/b000000x/

‡ J. Tian and J. Zhoucontributed equally to this work.

Recently, photosensitizers have been integrated with various nanomaterials including magnetic nanoparticles,[6] quantum dots,[7] gold vesicles,[8] upconvertion nanoparticles[9] and graphene oxide nanosheets[10] to construct highly efficient theranostic agents. While these agents show encouraging treatment results, there are still three main limitations. The inorganic or metallic nature of most nanomaterials has raised great concerns of potential toxicity to normal tissues. To solve the problem, polymer-based materials such as poly (lactic acid) and poly (ethylene oxide) with good biocompatibility are desired because they are typically nontoxic and naturally degraded into safe materials over time in body.[11] Another problem is the always-on property of photosensitizer which leads to high fluorescence background and therapeutic side effects. To overcome this defect, the design of photosensitizer with activatable functionality is an efficient way.[12] The photosensitizer should be switched off in noncancerous tissues but can be switched on by specific cancer-associated stimuli to effectively produce fluorescence and $^1O_2$. The third problem is that most currently available photosensitizers absorb visible light with limited penetration. Developing novel photosensitizer with strong absorbance in near-infrared (NIR, 700–1000 nm) region can effectively solve this problem,[13] which improves the homogeneity of the photosensitizer. These limitations and challenges have driven the further design of novel multifunctional photosensitizers and theranostic agents.

Our previous work reported a nanomicelle as a theranostic agent for simultaneous cancer imaging, PDT and therapeutic

monitoring[14]. However, the fluorescent excitation wavelength less than 700 nm for monitoring therapeutic efficacy and always-on photosensitizer for $^1O_2$ generation limit its application. In this regard, we attempt to rationally design a pH-activatable NIR photosensitizer for the preparation of theranostic agents. Herein, this goal is realized using a newly designed trifunctional photosensitizer, NEt_2Br_2BDP, which features an aza-boron-dipyrromethene (aza-BODIPY) structure substituted with diethylaminophenyl and bromophenyl (Fig. 1a). For *in vivo* application, NEt_2Br_2BDP is encapsulated in a cyclic RGD peptide-poly(ethylene glycol)-*block*-poly(lactic acid) (cRGD-PEG-PLA) and methoxyl poly(ethylene glycol)-*block*-poly(lactic acid) (mPEG-PLA) nanomicelle to form a theranostic nanoprobe (cRGD-NEt_2Br_2BDP NP). The nanoprobe keeps silence in the physiological pH environment at 7.4. With the help of cRGD, it can be selectively uptaken by $\alpha_v\beta_3$ integrin-rich tumor cells into the lysosomes, in which the nanoprobe is activated by acidic pH environment at 4.5–5.0 to produce 925-nm fluorescence for tumor discrimination and $^1O_2$ for tumor therapy under 808-nm irradiation. In addition, the therapeutic self-monitoring can be achieved synchronously by monitoring the fluorescence decrease. This work provides an effective theranostic nanoprobe for highly selective *in vivo* tumor imaging, efficient PDT and therapeutic self-monitoring in the NIR region.

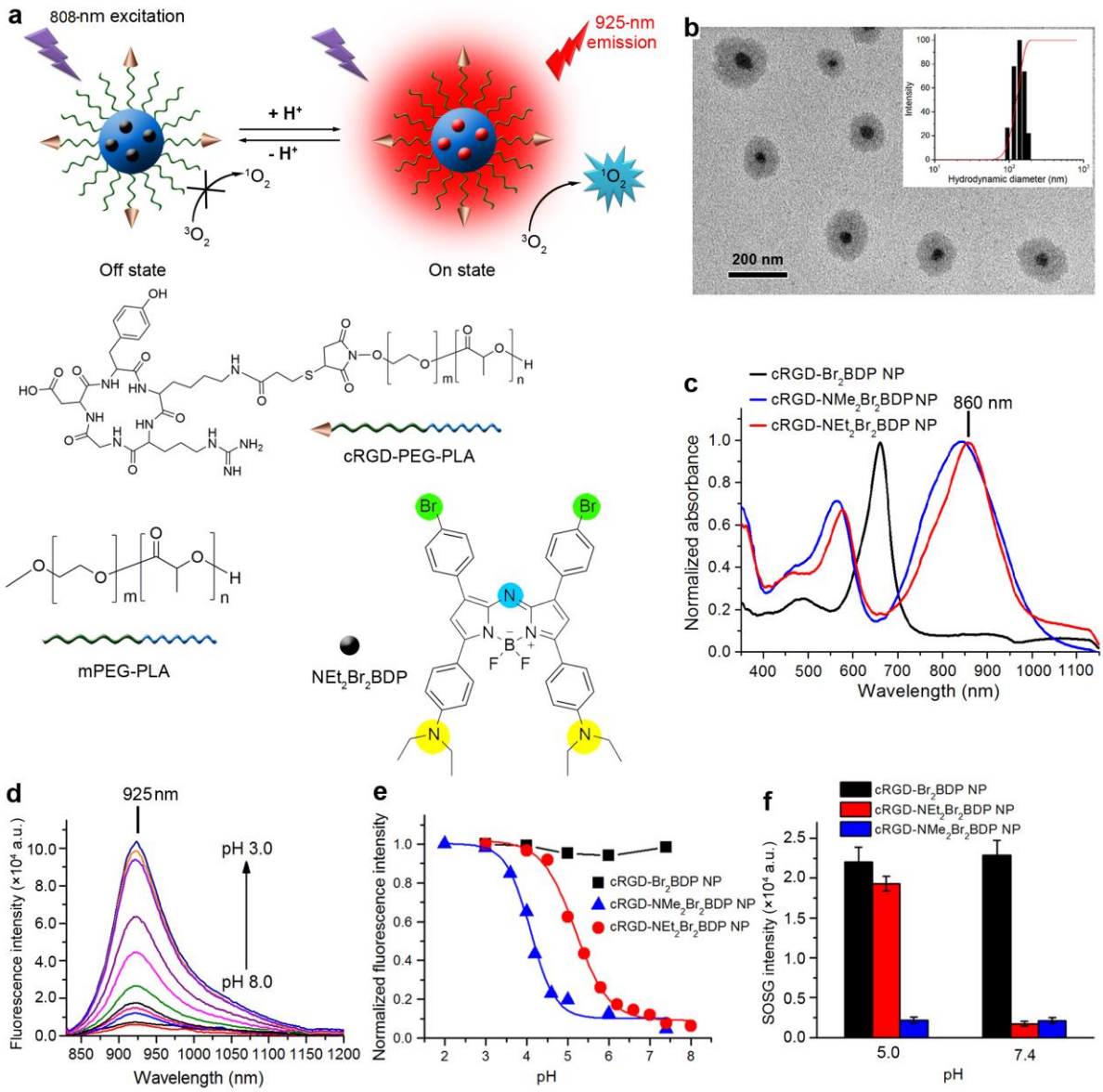

Fig. 1 Structure, characterization and optical properties of cRGD-NEt_2Br_2BDP NP. (a) Structures and pH-activatable generation of fluorescence and $^1O_2$ by cRGD-NEt_2Br_2BDP NP. (b) TEM image of cRGD-NEt_2Br_2BDP NP negatively stained with 2.0% sodium phosphotungstate. Inset: Size distribution of cRGD-NEt_2Br_2BDP NP determined with DLS. (c) Normalized UV-VIS-NIR absorption spectra of cRGD-Br_2BDP NP, cRGD-NMe_2Br_2BDP NP and cRGD-NEt_2Br_2BDP NP. (d) NIR fluorescence spectra of cRGD-NEt_2Br_2BDP NP at pH 8.0, 7.4, 7.0, 6.6, 6.2, 5.8, 5.4, 5.0, 4.5, 4.0 and 3.0. (e) pH titration curves of fluorescence intensity of cRGD-Br_2BDP NP at 685 nm, cRGD-NMe_2Br_2BDP NP at 910 nm and cRGD-NEt_2Br_2BDP NP at 925 nm. (f) $^1O_2$ generation of cRGD-Br_2BDP NP, cRGD-NMe_2Br_2BDP NP and cRGD-NEt_2Br_2BDP NP at pH 5.0 and 7.4 determined by SOSG fluorescence intensity at 525 nm.

Cite this: DOI: 10.1039/c0xx00000x

www.rsc.org/xxxxxx

ARTICLE TYPE

Results and discussion

Photophysical properties of NEt_2Br_2BDP

Owing to the favourable spectroscopic properties such as high molar absorption coefficient, narrow emission band and excellent photostability,[15] aza-BODIPY was chosen as the matrix of photosensitizer NEt_2Br_2BDP. The diethylaminophenyl was introduced to the structure of aza-BODIPY as a reactive moiety for pH-activatable NIR $^1O_2$ generation and fluorescence, and bromophenyl was imported to increase the $^1O_2$ generation efficiency upon pH activation (Scheme S1) in virtue of the heavy atom effect that enhances intersystem crossing of the excited energy.[16] For comparisons, the analogues with phenyl (Br_2BDP) or dimethylaminophenyl (NMe_2Br_2BDP) into the bromophenyl-substituted aza-BODIPY were also synthesized (ESI†). The absorption spectrum of NEt_2Br_2BDP displayed a strong peak at 850 nm with a molar absorption coefficient ε of 8.64×10^4 M^{-1} cm^{-1} and two weak peaks at 575 nm ($\varepsilon = 4.26 \times 10^4$ M^{-1} cm^{-1}) and 324 nm ($\varepsilon = 2.62 \times 10^4$ M^{-1} cm^{-1}) (Fig. S1†). The maximum absorption of Br_2BDP and NMe_2Br_2BDP was at 655 nm ($\varepsilon = 8.22 \times 10^4$ M^{-1} cm^{-1}) and 822 nm ($\varepsilon = 8.51 \times 10^4$ M^{-1} cm^{-1}), respectively, indicating that introduction of aniline moiety significantly promoted the red shift of absorption.

Characterization and pH-activatable NIR fluorescence of cRGD-NEt_2Br_2BDP NP

Compared to direct administration of free NEt_2Br_2BDP, its encapsulation in cRGD functionalized nanomicelle (Fig. 1a) *via* an emulsion/solvent evaporation method[14] provided distinct advantages, including better tumor accumulation, improved solubility and sustained drug-release kinetics.[17] The molecular weights (Mw) of the cRGD-PEG-PLA and mPEG-PLA were determined to be 7.1 and 4.6 KDa respectively by comparing the peak areas of PLA and PEG resonance at 5.20 ppm (-C(=O)-C**H**(-CH_3-)) and 3.65 ppm (-OC$\mathbf{H}_2$C$\mathbf{H}_2$-) in ^{1}H NMR spectra (Fig. S2 and S3†), respectively. The encapsulation efficiency (EE) and loading efficiency (LE) was measured to be 84.8% and 3.2% (Table S1†), respectively. The TEM image of cRGD-NEt_2Br_2BDP NP showed well-dispersed spherical morphology with core-shell structure (Fig. 1b). Its average hydrodynamic diameter measured by dynamic light scattering (DLS) was 138.4 ± 17.3 nm (Fig. 1b), which did not change for at least four weeks (Fig. S4†), indicating the colloidal stability of nanoprobe. After encapsulation in the nanomicelle, the structured absorption of NEt_2Br_2BDP was maintained well (Fig. 1c), indicating the structural integrity. The 10-nm red shift of the absorption peak of cRGD-NEt_2Br_2BDP NP in PBS compared with both free NEt_2Br_2BDP and cRGD-NEt_2Br_2BDP NP in $CHCl_3$ (Fig. S5†) was attributed to the entrapment of NEt_2Br_2BDP inside the core of nanomicelle.[18] The cRGD-NEt_2Br_2BDP NP could be excited at NIR region to produce a NIR 925-nm fluorescent emission which was highly pH-dependent (Fig. 1d). The 925-nm fluorescence was almost undetectable at pH 7.4 with a fluorescence quantum yield Φ_F less than 0.002 using indocyanine green (ICG) in DMSO (Φ_F = 0.13) as a standard (see Supporting Information). The fluorescence quenching was due to the photoinduced electron transfer from the aniline moiety to the excited fluorophore.[19] With the increase of solution acidity, the 925-nm fluorescence increased distinctly, which showed a Φ_F of 0.18 at pH 4.5. The maintained absorption and pH-dependent fluorescence of the probe indicated a porous structure, which ensured the access of proton to NEt_2Br_2BDP. The standard fluorescence pH titration gave an apparent pK_a value of 5.2 (Fig. 1e), which suggested that the cRGD-NEt_2Br_2BDP NP was pH activatable and could response physiologically acidic pH range of 4.5–6.9[20] with high sensitivity. Upon 635-nm excitation, the cRGD-Br_2BDP NP could emit fluorescence at 685 nm (Fig. S6†), which was stable to the solution pH (Fig. 1e), indicating that cRGD-Br_2BDP NP could be used as an always-on control. Different from the designed cRGD-NEt_2Br_2BDP NP, the pH-dependent fluorescence of cRGD-NMe_2Br_2BDP NP occurred at 910 nm (Fig. S7†), which showed a p*K*a value of 4.1 (Fig. 1e), not matching the physiologically acidic pH range. Thus cRGD-NMe_2Br_2BDP NP was used as an always-off control.

pH-activatable generation of $^1O_2$

The pH controllable release of $^1O_2$ induced by cRGD-NEt_2Br_2BDP NP under 808-irradiation was evaluated with singlet oxygen sensor green (SOSG) as a $^1O_2$ indicator. This indicator can emit strong fluorescence at 525 nm upon reaction with $^1O_2$. After exposing the mixed cRGD-NEt_2Br_2BDP NP and SOSG solution at pH 7.4 under 808nm irradiation for 300 s, the SOSG fluorescence intensity at 525 nm did not increase, while the fluorescence intensity of SOSG increased greatly at pH 5.0 under 808 nm irradiation (Fig.S8-S10†). The SOSG intensity enhanced 11 folds from pH 5.0 to 7.4 (Fig. 1f). The singlet oxygen quantum yields (Φ_Δ) of cRGD-NEt_2Br_2BDP NP at different pHs could be measured using a 1,3-diphenylisobenzofuran (DPBF) method (Fig. S11).[19] The results indicated that the Φ_Δ increased from 0.05 at pH 7.4 to 0.56 at pH 5.0, which further confirmed the pH controllable release of $^1O_2$. As the always-on cRGD-Br_2BDP NP or always-off cRGD-NMe_2Br_2BDP NP controls, they showed ignorable pH impact on the SOSG fluorescence intensity after irradiation (Fig. 1f). These results demonstrated that cRGD-NEt_2Br_2BDP NP was a potential and promising pH-activatable theranostic agent for cancer treatment.

Sensitivity of cRGD-NEt_2Br_2BDP NP-based NIR imaging

NIR fluorescence facilitates bioimaging and detection because it involves less interference from tissue autofluorescence.[21] The sensitivity of the cRGD-NEt_2Br_2BDP NP-based fluorescence imaging was studied in BALB/c nude mice (Fig. 2a). The $\alpha_v\beta_3$ integrin-rich human glioblastoma U87MG tumor cells were used as model and labelled with cRGD-NEt_2Br_2BDP NP. After 500, 200 and 50 cRGD-NEt_2Br_2BDP NP-labelled U87MG cells were

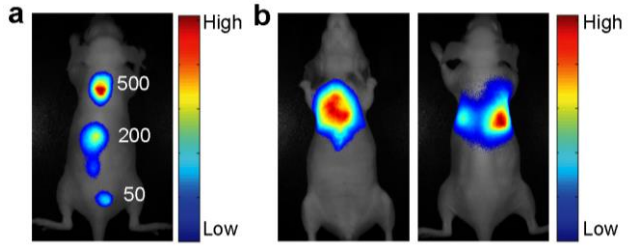

Fig. 2 *In vivo* NIR fluorescence imaging sensitivity and depth of U87MG cells labelled with cRGD-NEt_2Br_2BDP NP. (a) Imaging sensitivity with reduced cRGD-NEt_2Br_2BDP NP-loaded U87MG cell numbers (500, 200 and 50) injected on the back of a nude mouse. (b) Thoracic and dorsal views of a nude mouse with intralumen injection of 1×10^4 cRGD-NEt_2Br_2BDP NP-loaded U87MG cells.

subcutaneously injected on the back of a nude mouse, and the mouse was subjected to imaging on a Maestro EX in-vivo imaging system. The U87MG cells displayed distinct fluorescence at the injection sites while no fluorescence signal was observed in other regions of the mouse body. The detectable cell number down to 50 cells was lower than the detection limit of 98 cells of infrared-emitting long-persistence luminescent nanoparticles-based cell tracking,[22] were clearly visualized, revealing the good sensitivity. The sensitivity was attributed to NIR fluorescence by overwhelming the interference from tissue autofluorescence. The penetrability of NIR fluorescence was further examined with a mouse treated with intralumen injection of cRGD-NEt_2Br_2BDP NP-labelled U87MG cells (Fig. 2b), which indicated that the NIR fluorescence could penetrate through the thoracic cavity of the living nude mouse and was detectable on its back side. The thickness of the mouse body was about 2 cm, and the penetration depth of the pH activatable cRGD-NMe_2Br_2BDP NP was at least 1 cm. These results confirmed that the excitation and emission light of the nanoprobe possessed acceptable penetration depth for the imaging of tumor cells.

In vivo imaging on subcutaneous U87MG tumor-bearing mice

The blood circulation curve of cRGD-NEt_2Br_2BDP NP in mice showed the biphasic clearance profile with a rapid clearance during the first 5 h followed by a continuous and slow elimination rate (Fig. S12†). The blood circulation half-life was found to be 4.8 h, indicating a long persistence of cRGD-NEt_2Br_2BDP NP in bloodstream to corroborate the stability *in vivo*. The *in vivo* tumor imaging was investigated in mice bearing subcutaneous U87MG tumor xenograft. The U87MG tumor-bearing mice were intravenously injected with cRGD-NEt_2Br_2BDP NP, cRGD-NMe_2Br_2BDP NP or cRGD-ICG NP, and implemented with *in vivo* imaging at different time points to explore the function of pH activation (Fig. 3a).

To inquire the targeting of cRGD, the U87MG tumor-bearing mice were also injected intravenously with NEt_2Br_2BDP NP without cRGD functionalization to perform the imaging (Fig. 3b). As an additional control, a blocking dose of cRGD was injected before the cRGD-NEt_2Br_2BDP NP administration (Fig. 3b). After injection for 2 h, the tumor tissue in NP-treated mouse could be distinguished from the surrounding normal tissues (Fig. 3a). The

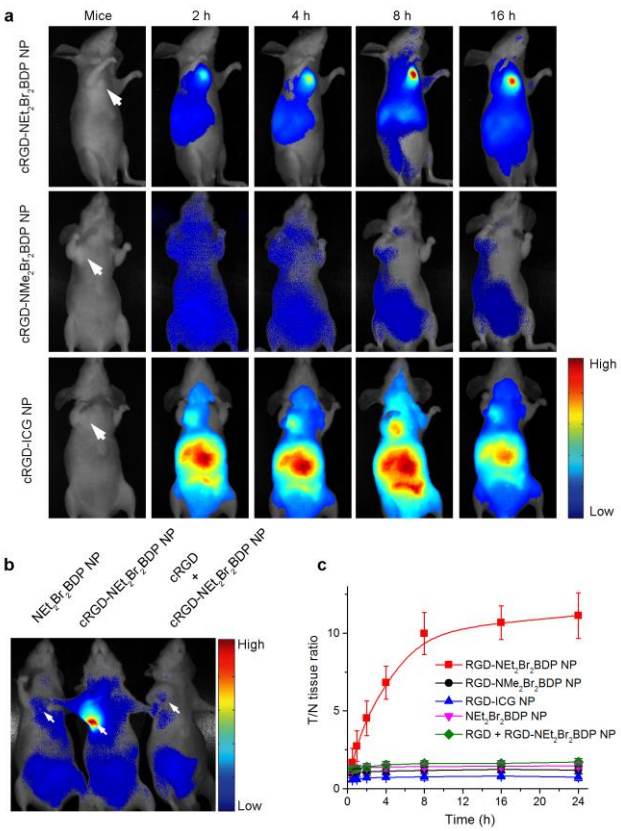

Fig. 3 *In vivo* NIR fluorescence tumor imaging. The arrows show the tumor sites. (a) Time-dependent *in vivo* NIR fluorescence images of subcutaneous U87MG tumor-bearing mice after intravenous injection of 20 mg kg^{-1} pH-activatable cRGD-NEt_2Br_2BDP NP, always-off cRGD-NMe_2Br_2BDP NP as a negative control or always-on cRGD-ICG NP as a positive control. (b) *In vivo* NIR fluorescence image of subcutaneous U87MG tumor-bearing mice at 8 h post-injection of 20 mg kg^{-1} NEt_2Br_2BDP NP or cRGD-NMe_2Br_2BDP NP, and competition group. In competition group, a blocking dose of cRGD peptide (25 mg kg^{-1}) is injected 30 min before cRGD-NEt_2Br_2BDP NP administration. (c) *In vivo* time-dependent T/N tissue ratios after injection of different nanoprobes. Data are presented as means ± SD (n = 6).

ratioof fluorescence at tumor to normal tissue (T/N tissue ratio) increased gradually and reached a maximum (10 folds) at 8-h postinjection, and the high fluorescence contrast could be maintained even after 16-h postinjection (Fig. 3c), demonstrating the targeted delivery, pH-activatable fluorescence and long retention of cRGD-NEt_2Br_2BDP NP in tumor tissue. Ex vivo imaging clearly showed that the specific activation of cRGD-NEt_2Br_2BDP was at the tumor tissue over other organs including heart, liver, spleen, lung, kidney, stomach, intestine and muscle (Fig. S13†). Conversely, the always-off cRGD-NMe_2Br_2BDP NP treated mouse as a negative control showed negligible fluorescence in tumor (Fig. 3a) and other organs (Fig. S14†), which could be explained with the pKa of 4.1, at which cRGD-NMe_2Br_2BDP NP could not be activated. For always-on cRGD-ICG NP treated mouse as a positive control, although the tumor displayed fluorescence, the interferences from normal tissues

were serious (Fig. 3a), and the high fluorescence background was also observed in lung, liver and kindneys (Fig. S15†), leading to a low T/N tissue ratio (less than 0.8) at all time points (Fig. 3c). Compared to the always-off cRGD-NMe_2Br_2BDP NP and always-on cRGD-ICG NP, the 10-fold T/N tissue ratio verified the advantages of pH-activatable function of cRGD-NEt_2Br_2BDP NP by reducing the signal background from the normal tissues. For the NEt_2Br_2BDP NP and free cRGD competition controls, no fluorescence was observed in tumor (Fig. 3b), which confirmed the contribution of cRGD in tumor targeting for pH activation.

In vivo PDT evaluation

For *in vivo* PDT treatment, the U87MG tumor-bearing mice were randomly divided into 6 groups with untreated (group 1) and treated with irradiation (group 2), cRGD-NEt_2Br_2BDP NP injection (group 3), cRGD-NEt_2Br_2BDP NP injection and then irradiation (group 4), NEt_2Br_2BDP NP injection and then irradiation (group 5), or cRGD-NMe_2Br_2BDP NP and then irradiation (group 6). After 8 h postinjection, the corresponding treatments were conducted. The irradiation was performed with a NIR 808 nm laser at an irradiance of 100 mW cm^{-2} for 300 s. The therapeutic effects after treatment were assessed by monitoring the change of relative tumor volumes (Fig. 4a) and hematoxylin and eosin (H&E) staining (Fig. 4b). No tumor growth inhibition or tumor tissue necrosis was observed for the group of mice in the absence of irradiation or/and cRGD-NEt_2Br_2BDP NP, which indicated that irradiation with a low irradiance of 100 mW cm^{-2} had little photothermal effect and the cRGD-NEt_2Br_2BDP NP had little dark toxicity. In marked contrast, the tumor growth for group 4 was remarkably suppressed, and the tumor tissue showed obvious necrosis, indicating that cRGD-NEt_2Br_2BDP NP could be effectively activated under NIR irradiation to produce a strong phototoxicity to tumor. Group 5 did not show therapeutic effect in tumor tissue due to the lack of cRGD targeting for pH activation, and group 6 showed rapid tumor growth because the cRGD-NMe_2Br_2BDP NP could not be activated by physiologically acidic pH under irradiation. These results

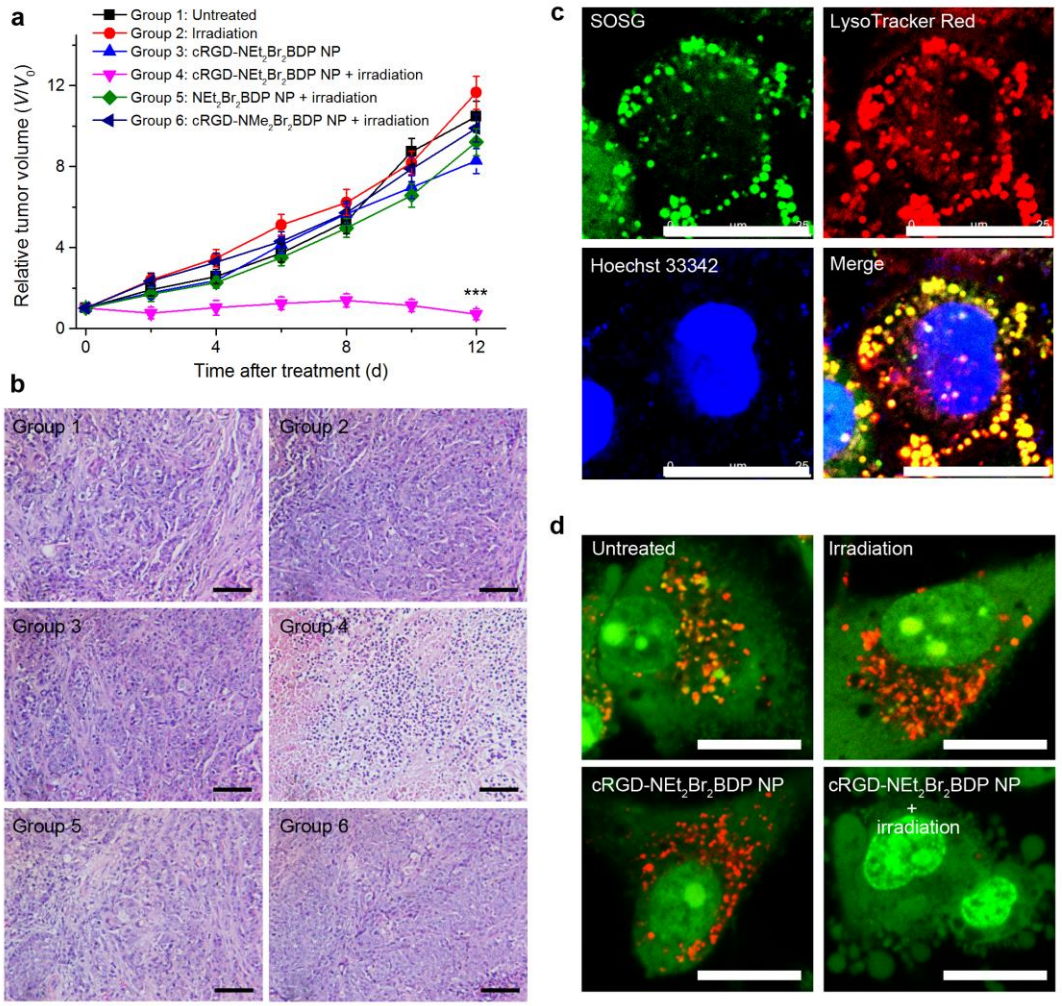

Fig 4. *In vivo* and *in vitro* NIR PDT against tumor.(a) Tumor growth curves of different treatment groups. Data are presented as means ± SD (n = 6, ***P< 0.001 compared to other groups using One-way ANOVA). (b) H&E stained images of tumor tissue sections from different groups at 8 d after treatment. Scale bars: 100 μm. (c) Subcellular localization of $^1O_2$ generated during cRGD-NEt_2Br_2BDP NP-mediated PDT with SOSG, LysoTracker Red and Hoechst 33342 staining. Scale bars: 25 μm. (d) Lysosomal stability observed with confocal fluorescence images of AO-stained U87MG cells after different treatments. Scale bars: 20 μm.

Cite this: DOI: 10.1039/c0xx00000x

www.rsc.org/xxxxxx

ARTICLE TYPE

confirmed the high therapeutic effect of cRGD-NEt_2Br_2BDP NP-mediated PDT.

The potential toxicity or side effects is always a great concern for theranostic agents used in medicine. At the cellular level, the NEt_2Br_2BDP before and after irradiation showed negligible toxicity (Fig. S16†). The mice treated with the NP-mediated PDT did not show apparent body weight loss (Fig. S17†). At 12 days after treatment, the PDT-treated mice and the age-matched healthy mice without treatment were sacrificed, and the major organs including heart, liver, spleen, lung, and kidney were collected for H&E staining to evaluate toxic effect. No noticeable sign of organ damage was observed from H&E-stained organ slices (Fig. S18†), which suggested the safety of cRGD-NEt_2Br_2BDP NP for *in vivo* PDT application.

Therapeutic mechanism of cRGD-NEt_2Br_2BDP NP-mediated PDT

In order to understand the therapeutic mechanism down to the subcellular level, the cRGD-NEt_2Br_2BDP NP-loaded U87MG cells were incubated with SOSG to study the subcellular localization of $^1O_2$. After 808 nm irradiation, strong SOSG fluorescence was observed which overlapped with LysoTracker Red (Fig. 4c), suggesting that $^1O_2$ generation was occurred in lysosomes. The previous works had demonstrated that $^1O_2$ production in lysosome induced lysosomal membrane permeabilization and subsequent release of cathepsins into cytosol to trigger cell-death pathways.[14,19] To further confirm the lysosomal destruction, acridine orange (AO) was employed as an integrity indicator of lysosome, which emits red fluorescence in lysosome and green fluorescence in cytosol and nucleus.[23] The lysosomes in U87MG cells displayed bright red fluorescence in the absence of cRGD-NEt_2Br_2BDP NP or/and irradiation (Fig.4d), suggesting that the lysosomal compartments were intact. After the cRGD-NEt_2Br_2BDP NP-loaded cells were irradiated, the red AO fluorescence disappeared (Fig. 4d), which indicated the destruction of lysosomal membrane. After U87MG cells were treated with always-off cRGD-NMe_2Br_2BDP NP, the irradiation with 808 nm laser did not damage the lysosomes (Fig. S19a†), which excluded the photothermal effect during irradiation. Moreover, the addition of vitamin C as a $^1O_2$ scavenger could efficiently prevent the damage to lysosome (Fig. S19b†). Therefore, the generated $^1O_2$ from the cRGD-NEt_2Br_2BDP NP-mediated PDT induced the cell death in alysosome-associated pathway.

Therapeuticself-monitoring

Owing to the intrinsic property of pH-activatable fluorescence of cRGD-NEt_2Br_2BDP NP, the function of therapeutic self-monitoring during the PDT process could be realized by fluorescence imaging (Fig. 5a). Two groups of mice bearing U87MG tumor were intravenously injected with the nanoprobe. After 8 h injection, they displayed a more than 10-fold T/N tissue ratio (Fig. 5b). With the pH-activatable fluorescence guiding, the group of mice was irradiated with an 808 nm laser at 100

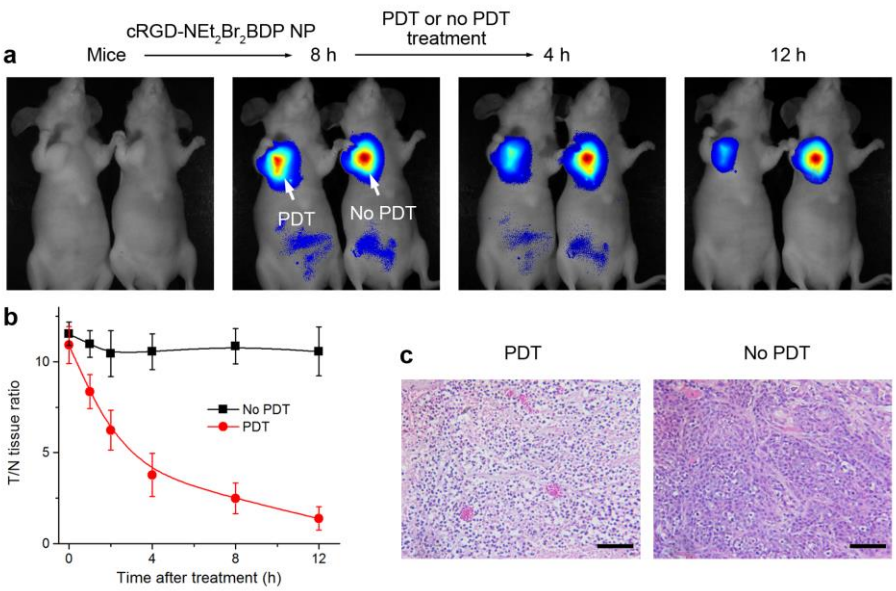

Fig. 5 *In situ* and real-time self-monitoring of PDT efficacy. (a) *In vivo* PDT and therapeutic monitoring on subcutaneous U87MG tumor-bearing mice with cRGD-NEt_2Br_2BDP NP. After 8 h post-injection, the 808-nm irradiation is implemented to the tumor of left mouse, and the tumor on right mouse is kept in dark as a control. (b) Time-dependent T/N tissue ratios of subcutaneous U87MG tumor-bearing mice with or without PDT. Data are presented as means ± SD (n = 6). (c) H&E stained images of the U87MG tumor tissue from the mice treated with or without PDT. Scale bars: 100 μm.

Cite this: DOI: 10.1039/c0xx00000x

www.rsc.org/xxxxxx

ARTICLE TYPE

mW cm^{-2} for 300 s, and another group of mice was kept in dark as a control. After irradiation, the therapeutic self-monitoring was performed by observing the fluorescence change of cRGD-NEt_2Br_2BDP NP. The fluorescence intensity from the irradiated tumor decreased gradually (Fig. 5a) and almost disappeared with a 1.4-fold T/N tissue ratio after 12 h (Fig. 5b). In contrast, the changes in both fluorescence (Fig. 5a) and T/N tissue ratio (Fig. 5b) for the unirradiated tumor were ignorable over the same period. In order to investigate the physiological transformation along with the fluorescent change after PDT, H&E staining of the two tumors was performed. Prominent necrosis was observed in the PDT-treated tumor tissue, while necrosis was indiscernible in the unirradiated tumor (Fig. 5c). Therefore, the cRGD-NEt_2Br_2BDP NP displayed not only highly selective tumor imaging and effective therapy functions, but also a self-monitoring capability for the evaluation of therapeutic efficacy.

Experimental section

Preparation and characterization of cRGD-NEt_2Br_2BDP NP

An emulsion/solvent evaporation method was used for the preparation of cRGD-NEt_2Br_2BDP NP.[14] In brief, 21 mg of cRGD-PEG-PLA and mPEG-PLA copolymers with a mixing ratio of 5% (w/w%) and 0.8 mg NEt_2Br_2BDP were dissolved in 2 mL CH_2Cl_2, which was then added to 4 mL of 2% Pluronic® F-127 aqueous solution. The mixture was sonicated using a probe sonicator (Scientz Biotechnology Co. Ltd., China) for 30 s at 180 W output. The formed emulsion was added dropwise to 20 mL of a magnetically stirred 0.5% Pluronic® F-127 aqueous solution. After stirring for 1 h, the remaining organic solvent was removed in a rotary evaporator at reduced pressure at 30 ℃. The cRGD-NEt_2Br_2BDP NP solution was filtrated through a Millipore syringe filter (pore size 0.45 μm) to remove unencapsulated NEt_2Br_2BDP aggregates and further purified by centrifugation at 21,000 × *g* for 15 min using a centrifugal filter with cutoff Mw of 100 kDa (Millipore, MA). After purification the cRGD-NEt_2Br_2BDP NP solution was freeze-dried. Similar procedures were used to prepare the cRGD-Br_2BDP NP, cRGD-NMe_2Br_2BDP NP, cRGD-ICG NP and NEt_2Br_2BDP NP, in which the nanocarrier was composed of mPEG-PLA. The EE and LE of photosensitizer loaded in the cRGD functionalized nanomicelle were determined by UV−VIS−NIR absorption spectroscopy. The EE and LE were expressed according to the following formulas: EE (%) = ((weight of loaded photosensitizer)/(weight of initially added photosensitizer)) × 100; LE (%) = ((weight of loaded photosensitizer)/(total weight of nanomicelle)) × 100. DLS and TEM measurements were performed to examine the size distribution and morphology of cRGD-NEt_2Br_2BDP NP.

In vivo tumor imaging

All animal operations were in accord with institutional animal use and care regulations approved by the Model Animal Research Center of Nanjing University (MARC). Specific pathogen-free (SPF) BALB/c nude mice, 5–6 weeks of age, were purchased from Shanghai Laboratory Animal Center, Chinese Academy of Sciences (SLACCAS) and bred in an axenic environment. Glioblastoma tumor models were established in BALB/c nude mice by injecting 1 × 10^6 U87MG cells subcutaneously into the selected positions. Tumors were then allowed to grow to 8−10 mm in diameter. For blood circulation time assay of cRGD-NEt_2Br_2BDP NP, the mice were fasted but had free access to water for 16 h, and then intravenously injected with 20 mg kg^{-1} cRGD-NEt_2Br_2BDP NP *via* tail vein. After injection for 0.5, 1, 3, 6, 12, 24 and 48 h, these mice were sacrificed, respectively, and the blood samples were obtained. With a standard curve method, the blood circulation time of the cRGD-NEt_2Br_2BDP NP was determined by measuring the fluorescence of cRGD-NEt_2Br_2BDP NP under acidic condition. To demonstrate the contribution of pH activation, 20 mg kg^{-1} pH-activatable cRGD-NEt_2Br_2BDP NP, always-off cRGD-NMe_2Br_2BDP NP or always-on cRGD-ICG NP was intravenously injected into U87MG tumor-bearing mice (n = 6) *via* a tail vein. *In vivo* tumor imaging was then performed on a Maestro EX in vivo imaging system with an excitation of 735 nm and collected emission range of 800−950 nm at 2, 4, 8 and 16-h postinjection. At 24 h postinjection, the mice were euthanized to obtain the organs and tumor tissues for imaging. To elucidate the role of $\alpha_v\beta_3$-mediated endocytosis, a group of mice (n = 6) were intravenously injected with 20 mg kg^{-1} NEt_2Br_2BDP NP for 8 h and another group of mice (n = 6) were intravenously injected with cRGDyk (25 mg kg^{-1}) 30 min before cRGD-NEt_2Br_2BDP NP administration. During the injection and image acquisition process, the mice were anesthetized with 2.5% isoflurane in oxygen delivered at a flow rate of 1.5 L min^{-1}. T/N tissue ratios were determined by comparing the average fluorescence intensities in the tumor and the whole body except the tumor site using Maestro 3.0 software.

In vivo PDT

In vivo cRGD-NEt_2Br_2BDP NP-mediated PDT was performed using U87MG tumor-bearing mice. The mice were randomly divided into 6 groups for the following treatments and each group contained six mice: group 1, untreated; group 2, irradiated with 808 nm laser for 300 s at an irradiance of 100 mW cm^{-2} (irradiation); group 3, intravenously injected with 20 mg kg^{-1} cRGD-NEt_2Br_2BDP NP for 8 h (cRGD-NEt_2Br_2BDP NP); group 4, intravenously injected with 20 mg kg^{-1} cRGD-NEt_2Br_2BDP NP for 8 h and irradiated with 808 nm laser at an irradiance of 100 mW cm^{-2} for 300 s (cRGD-NEt_2Br_2BDP NP + irradiation); group 5, intravenously injected with 20 mg kg^{-1} NEt_2Br_2BDP NP for 8 h and irradiated with 808 nm laser at an irradiance of 100 mW cm^{-2} for 300 s (NEt_2Br_2BDP NP + irradiation); group 6, intravenously injected with 20 mg kg^{-1} cRGD-NMe_2Br_2BDP NP for 8 h and irradiated with 808 nm laser at an irradiance of 100 mW $cm^{-2}$for 300 s (cRGD-NMe_2Br_2BDP NP + irradiation). The

mice from different treatment groups were monitored by measuring the tumor volume every two days for 12 days after treatment. The greatest longitudinal diameter (length) and the greatest transverse diameter (width) of each tumor were determined using a vernier caliper, and the tumor volume was calculated using length $\times$ width^2 $\times$ 0.5.[24]

***In vivo* therapeutic self-monitoring**

For self-monitoring of therapeutic efficacy, two groups of mice bearing U87MG tumor were intravenously injected with 20 mg kg^{-1} cRGD-NMe$_2$Br$_2$BDP NP *via* a tail vein. At 8-h postinjection, one group of mice (n = 6) were irradiated with 808 nm laser at an irradiance of 100 mW cm^{-2} for 300 s and another group of mice (n = 6) were kept in the dark as a control. The therapeutic monitoring was performed *in vivo* by observing the fluorescence change after irradiation by Maestro EX in vivo imaging system. The mice were sacrificed at 24 h post irradiation to examine the histopathology of tumors by H&E staining under a BX51 optical microscope (Olympus, Japan) in a blinded fashion by a pathologist.

Conclusions

This work successfully synthesizes an effective theranostic nanoprobe named as cRGD-NEt$_2$Br$_2$BDP NP to achieve highly selective *in vivo* tumor imaging, efficient PDT and therapeutic self-monitoring in the NIR region by encapsulating a newly designed trifunctional photosensitizer NEt$_2$Br$_2$BDP in the cRGD-functionlized nanomicelle. The cRGD-NEt$_2$Br$_2$BDP NP with little dark toxicity but strong phototoxicity can target to tumor cells *via* cRGD and be activated by physiologically acidic pH to produce fluorescence and $^1O_2$ for theranostics. The fascinating advantage of nanoprobe is the NIR implementation beyond 800 nm, which significantly improves the imaging sensitivity and increases penetration depth for PDT *via* a lysosomal cell-death pathway. By monitoring the fluorescence decrease in tumor region after PDT, the therapeutic efficacy is reflected *in situ* and in real time, which provides a valuable and convenient self-feedback function for PDT efficacy tracking. Therefore, this rationally designed and carefully engineered nanoprobe offers a new paradigm for precise tumor theranostics and may provide novel opportunities for future clinical cancer treatment.

Acknowledgements

This study was supported by the National Basic Research Program (2014CB744501), National Science Fund for Creative Research Groups (21121091), National Natural Science Foundation of China (21135002, 91413118, 21322506, 91213301, 21371090) and Priority development areas of The National Research Foundation for the Doctoral Program of Higher Education of China (20130091130005).

Notes and references

1 (a) E. K. Lim, T. Kim, S. Paik, S. Haam, Y. M. Huh and K. Lee, *Chem. Rev*., 2015, **115,** 327–394; (b) J. H. Ryu, S. Lee, S. Son, S. H. Kim, J. F. Leary, K. Choi and I. C. Kwon, *J. Control. Release*, 2014, **28**, 477–484; (c) B. T. Luk andL. Zhang, *ACS Appl. Mater. Interfaces*, 2014, **24**, 21859–21873.

2 (a) S. S. Lucky, K. C. Soo and Y. Zhang, *Chem. Rev*., 2015, **115**, 1990–2042; (b) C. R. Policard, *Soc. Biol*., 1924, **91**, 1423–1424; (c) R. L. Lipson, E. J. Baldes and M. J. Gray, *Cancer*, 1967, **20**, 2255–2257; (d) U. Schmidt-Erfurth, J. W. Miller, M. Sickenberg, H. Laqua, I. Barbazetto, E. S. Gragoudas, L. Zografos, B. Piguet, C. J. Pournaras, G. Donati, A. M. Lane, R. Birngruber, H. van den Berg, H. A. Strong, U. Manjuris, T. Gray, M. Fsadniand N. M. Bressler, *Arch. Ophthalmol*., 1999, **117**, 1177–1187.

3 (a) D. E. Dolmans, D. Fukumura and R. K. Jain, *Nat. Rev. Cancer*, 2003, **3**, 380–387; (b) A. P. Castano, P. Mroz and M. R. Hamblin, *Nat. Rev. Cancer*, 2006, **6**, 535–545.

4 (a) X. He, X. Wu, K. Wang, B. Shi and L. Hai, *Biomaterials*, 2009, **30**, 5601–5609; (b) P. Huang, J. Lin, X. Wang, Z. Wang, C. Zhang, M. He, K. Wang, F. Chen, Z. Li, G. Shen, D. Cui and X. Chen, *Adv. Mater*., 2012, **24**, 5104–5110.

5 (a) B. C. Wilson, M. S. Patterson and L. Lilge, *Laser Med. Sci*., 1997, **12**, 182–199; (b) J. C. Finlay, D. L. Conover, E. L. Hull and T. H. Foster, *Photochem. Photobiol*., 2001, **73**, 54–63; (c) M. Mitsunaga, M. Ogawa, N. Kosaka, L. T. Rosenblum, P. L. Choyke and H. Kobayashi, *Nat. Med.*, 2011, **17**, 1685–1691; (d) M. T. Jarvi, M. J. Niedre, M. S. Patterson and B. C. Wilson, *Photochem. Photobiol*., 2006, **82**, 1198–1210.

6 P. Huang, Z. Li, J. Lin, D. Yang, G. Gao, C. Xu, L. Bao, C. Zhang, K. Wang, H. Song, H. Hu and D. Cui, *Biomaterials*, 2011, **32**, 3447–2458.

7 J. M. Tsay, M. Trzoss, L. Shi, X. Kong, M. Selke, M. E. Jung and S. Weiss, *J. Am. Chem. Soc.*, 2007, **129**, 6865–6871.

8 (a) B. Jang and Y. Choi, *Theranostics*, 2012, **2**, 190–197; (b) J. Lin, S. Wang, P. Huang, Z. Wang, S. Chen, G. Niu, W. Li, J. He, D. Cui, G. Lu, X. Chen and Z. Nie, *ACS Nano*, 2013, **7**, 5320–5329.

9 N. M. Idris, M. K. Gnanasammandhan, J. Zhang, P. C. Ho, R. Mahendran and Y. Zhang, *Nat. Med.*, 2012, **18**, 1580–1585.

10 (a) Y. Cho, H. Kim and Y. Choi, *Chem. Commun*., 2013, **49**, 1202–1204; (b) Y. Cho and Y. Choi, *Chem. Commun*., 2012, **48**, 9912–9914; (c) P. Rong, K. Yang, A. Srivastan, D. Kiesewetter, X. Yue, F. Wang, L. Nie, A. Bhirde, Z. Wang, Z. Liu, G. Niu, W. Wang and X. Chen, *Theranostics*, 2014, **4**, 229–239.

11 (a) C. Zhan, B. Gu, C. Xie, J. Li, Y. Liu and W. Lu, *J. Control. Release*, 2010, **143**, 136–142; (b) G. H. Xiang, G. B. Hong, Y. Wang, D. Cheng, J. X. Zhou and X. T. Shuai, *Int. J. Nanomedicine*, 2013, **8**, 4613–4622; (c) L. Gibot, A. Lemelle, U. Till, B. Moukarzel, A. F. Mingotaud, V. Pimienta, P. Saint-Aguet, M. P. Rols, M. Gaucher, F. Violleau, C. Chassenieux and P. Vicendo, *Biomacromolecules*, 2014, **15**, 1443–1455.

12 (a) Y. Choi, R. Weissleder and C. H. Tung, *Cancer Res*., 2006, **66**, 7225–7229; (b) G. Zheng, J. Chen, K. Stefflova, M. Jarvi, H. Li and B. C. Wilson, *Proc. Natl. Acad. Sci. U.S.A.*, 2007, **104**, 8989–8994; (c) J. F. Lovell, T. W. B. Liu, J. Chen and G. Zheng, *Chem. Rev.*, 2010, **110**, 2839–2857; (d) J. Kim, C. H. Tung and Y. Choi, *Chem. Commun.*, 2014, **50**, 10600–10603; (e) Y. Ichikawa, M. Kamiya, F. Obata, M. Miura, T. Terai, T. Komatsu, T. Ueno, K. Hanaoka, T. Nagano and Y. Urano, *Angew. Chem. Int. Ed.*, 2014, **53**, 6772–6775.

13 M. Ethirajan, Y. Chen, P. Joshi and R. K. Pandey, *Chem. Soc. Rev.*, 2011, **40**, 340–362.

14 J. Tian, L. Ding, H. X. Ju, Y. Yang, X. Li, Z. Shen, Z. Zhu, J. S. Yu and C. J. Yang, *Angew. Chem. Int. Ed*., 2014, **53**, 9544–9549.

15 (a) A. Diaz-Moscoso, E. Emond, D. L. Hughes, G. J. Tizzard, S. J. Coles and A. N. Cammidge, *J. Org. Chem.*, 2014, **79**, 8932–8936; (b) S. O. McDonnell and D. F. O'Shea, *Org. Lett.*, 2006, **8**, 3493–3496; (c)A. Loudet, R. Bandichhor, L. Wu and K. Burgess, *Tetrahedron*., 2008, **64**, 3642–3654.

16 A. Gorman,J. Killoran, C. O'Shea, T. Kenna, W. M. Gallagher and D. F. O'Shea, *J. Am. Chem. Soc.*, 2004, **126**, 10619–10631.

17 (a) J. A. Barreto, W. O'Malley, M. Kubeil, B. Graham, H. Stephan and L. Spiccia, *Adv. Mater.*, 2011, **23**, H18–H40; (b) S. M. Abdelghany, D. Schmid, J. Deacon, J. Jaworski, F. Fay, K. M. McLaughlin, J. A. Gormley, J. F. Burrows, D. B. Longley, R. F. Donnelly and C. J. Scott, *Biomacromolecules*, 2013, **14**, 302–310.

18 G. Raino,T. Stoferle, C. Park, H. C. Kim, I. J. Chin, R. D. Miller and R. F. Mahrt, *Adv. Mater.*, 2010, **22**, 3681–3684.

19 J. Tian, L. Ding, H. J. Xu, Z. Shen, H. Ju, L. Jia, L. Bao and J. S. Yu, *J. Am. Chem. Soc.*, 2013, **135**, 18850–18858.
20 C. Li, J. Xia, X. Wei, H. Yan, Z. Si and S. Ju, *Adv. Funct. Mater.*, 2010, **20**, 2222–2230.
21 S. A. Hilderbrand and R. Weissleder, *Curr.Opin. Chem. Biol.*, 2010, **14**, 71–79.
22 J. Shi, X. Sun, J. Li, H. Man, J. Shen, Y. Yu and H. Zhang, *Biomaterials*, 2014,**37**, 260–270.
23 H. Chen, L. Xiao,Y. Anraku, P. Mi, X. Liu, H. Cabral, A. Inoue, T. Nomoto, A. Kishimura, N. Nishiyama and K. Kataoka, *J. Am. Chem. Soc.*, 2014, **136**, 157–163.
24 D. M. Euhus, C. Hudd, M. C. LaRegina and F. E. Johnson, *J. Surg. Oncol*., 1986, **31**, 229–234.

Cite this: DOI: 10.1039/c0xx00000x

www.rsc.org/xxxxxx

ARTICLE TYPE

Table of contents

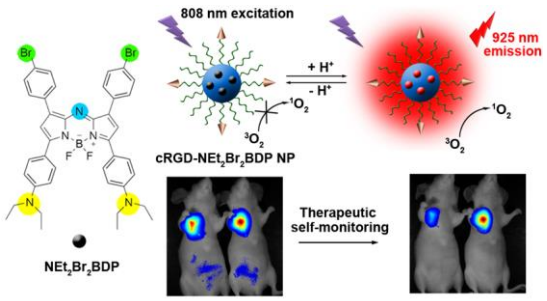

A trifunctional photosensitizer was designedto achieve highly selective near-infraed tumor imaging, efficient photodynamic therapy and therapeutic self-monitoring.